Food Hydrocolloids 162 (2025) 110904

Contents lists available at ScienceDirect

Food Hydrocolloids

journal homepage: www.elsevier.com/locate/foodhyd

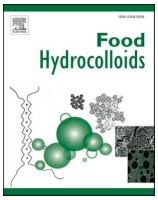

Development of soy protein isolate-chelator soluble pectin composite gels as extrusion-based 3D food printing inks: Effects of mingling strategy

Jin Xie [a,b], Jinfeng Bi [a,*], Xiaoxian Liu [b], Christophe Blecker [b], Nicolas Jacquet [b,***], Jian Lyu [a,**]

[a] Institute of Food Science and Technology, Chinese Academy of Agricultural Sciences, Key Laboratory of Agro-products Processing, Ministry of Agriculture and Rural Affairs, Beijing, 100193, China
[b] University of Liège, Gembloux Agro-Bio Tech, Unit of Food Science and Formulation, Avenue de la Faculté d'Agronomie 2B, Gembloux, B-5030, Belgium

ARTICLE INFO

Keywords:
Chelator soluble pectin
Soy protein isolate
Composite gel
Rheology
3D printing
Microstructure

ABSTRACT

This study explored the mingling strategy of soy protein isolate (SPI) and chelator-soluble pectin (CSP) to develop composite gels as extrusion-based 3D food printing inks. Specifically, the effect of various ratios of SPI and CSP (1:9, 3:7, 5:5, 7:3 and 9:1) on the composites' macrostructure and microstructure, physicochemical properties, and rheological behavior was systematically analyzed. Results showed that as the SPI concentration increased, S7C3 exhibited an appropriate particle size (215.10 μm), apparent viscosity and strong water holding capacity (T_{22a} = 3.18 ms), which could be identified as an entanglement gel. The backbone of SPI-CSP composites was primarily composed of closely linked C, O, and N, as revealed by SEM-energy dispersive X-ray spectroscopy, confirming the strong interaction between SPI-CSP and the formation of new composites. This result was further supported by the XRD and FT-IR analysis. Due to its superior viscosity and mechanical strength, S7C3 was the optimal formulation for 3D printing, providing highly precise printed structures. Furthermore, molecular docking revealed that the galacturonan ligand in CSP bound more effectively to 7 S with low binding energy (−6.8 kcal/mol) than to 11 S (−5.9 kcal/mol), contributing to the stabilization of the gel structure.

1. Introduction

3D printing, as an extrusion-based printing technology, is widely used to produce innovative foods with complex shapes, unique textures, and enhanced nutritional value. It can meet the specific dietary needs of diverse groups, including the elderly, children, and patients with special nutritional requirements (Vancauwenberghe, Verboven, Lammertyn, & Nicolaï, 2018; Wang, Jiang, et al., 2024). However, developing suitable edible food inks for 3D printing remains a challenge, as these inks require specific textural properties, such as excellent flow characteristics, rapid solidification and high fidelity and stability (Ahmadi Soufivand, Faber, Hinrichsen, & Budday, 2023).

In gel systems, interactions between proteins and pectins can modify the structural and surfactant properties (Zhang et al., 2024b), making them desirable for 3D printing food inks (Vancauwenberghe et al., 2018). When soy protein isolate (SPI) was combined with apricot polysaccharide, gelatinization and viscoelasticity were enhanced, leading to improved hardness and chewiness of 3D printed objects (Xu et al., 2023). Similarly, the addition of citrus pectin enhanced the structure and rheological properties of pea protein food ink, which was more suitable for 3D printing (Gu, Gu, Raghavan, & Wang, 2024). Taken together, the interaction between components plays a crucial role in determining the stability and rheological properties of food inks for 3D printing (Feng et al., 2024).

SPI, known for its excellent gelling and emulsification properties, is ideal for enhancing the mechanical strength of 3D-printed food structures (Chen et al., 2022). Chelating-solution pectin (CSP), a natural polysaccharide, is valued for its gelling, thickening, and stabilizing

* Corresponding author. Institute of Food Science and Technology, Chinese Academy of Agricultural Sciences, Key Laboratory of Agro-products Processing, Ministry of Agriculture and Rural Affairs, Beijing, 100193, China.
** Corresponding author. Institute of Food Science and Technology, Chinese Academy of Agricultural Sciences, Key Laboratory of Agro-products Processing, Ministry of Agriculture and Rural Affairs, Beijing, 100193, China
*** Corresponding author. University of Liège, Gembloux Agro-Bio Tech, Unit of Food Science and Formulation, Avenue de la Faculté d'Agronomie 2B, Gembloux, B-5030, Belgium
E-mail address: bjfcaas@126.com (J. Bi).

https://doi.org/10.1016/j.foodhyd.2024.110904
Received 8 October 2024; Received in revised form 20 November 2024; Accepted 30 November 2024
Available online 5 December 2024

abilities (Zhou et al., 2021). Its unique ability to interact with calcium ions and form stable gels makes CSP ideal for providing the textural qualities required for high-precision 3D food printing (Jiang et al., 2024; Xie, Bi, et al., 2024a). The increased pectin content within high internal phase emulsions significantly enhanced the viscosity and gel strength of the printed emulsions, which indicated the 3D-printed potentiality for meat (Bi et al., 2022). Taken together, as natural and nutrient-rich materials, SPI and pectin with excellent gel-forming and viscosity-controlled properties support the stable 3D printed food with high content of protein and dietary fiber, which also can offer the premise-controlled biocompatibility and customizable textures to caster the specific dietary needs (Gu, Gu, Raghavan, & Wang, 2024). However, the synergistic effects between SPI and CSP in 3D food printing remain underexplored. By mingling pectin with SPI, the gel properties were enhanced, which could be designed to meet the needs of individuals with special dietary requirements, such as those who have difficulty chewing or swallowing or those who do not consume sufficient high-protein foods.

Although SPI and pectin have been studied in various food applications, their synergistic effects in 3D food printing remain underexplored. By mingling pectin with SPI, the gel properties were enhanced, which could be designed to meet the needs of individuals with special dietary requirements, such as those who have difficulty chewing or swallowing or those who do not consume sufficient high-protein foods.

This study aims to explore the synergistic interactions between SPI and CSP by optimizing the ratio of SPI and CSP and developing a stable food ink for 3D printing. To achieve this, we analyzed the macro-physicochemical properties and microstructure features of SPI-CSP composite gels, identifying the optimal SPI to CSP ratio for 3D printing. We evaluated the appearance, particle size distribution, turbidity, and rheological properties to explore the effect of the mingling strategy on the gelling properties and stability of SPI-CSP composites. Additionally, X-ray diffraction (XRD), low-field nuclear magnetic resonance (LF-NMR), scanning electron microscopy (SEM) and SEM with energy dispersive X-ray spectroscopy (SEM-EDX) provided insights into the microstructure and elemental composition. The formation mechanism of SPI-CSP composites was revealed by both Fourier Transform infrared spectroscopy (FTIR) and molecular docking. This study not only provides insights into the interaction mechanism between SPI and CSP but also contributes to the development of SPI-CSP inks for 3D printing.

2. Materials and methods

2.1. Materials

Peaches of *Meirui* were chosen as the test material, which were harvested in Institute of Forestry and Pomology, Beijing Academy of Agriculture and Forestry Sciences. Ripened *Meirui* was selected, with 90.82 ± 2.40 % water content and 6.94 ± 0.31% soluble solids content. SPI (S300914, protein content ≥90 %, analytical grad) was obtained from Shanghai Yuanye Bio-Technology Co. Ltd (Shanghai, China). Bovine serum albumin (BSA) protein concentration assay kit was provided by Yuanye Bio-Technology Co. Ltd (Shanghai, China). All chemicals were analytical grade and purchased from Solaibao Technology Co., Ltd (Beijing, China).

2.2. Preparation of chelator soluble pectin

CSP was extracted from peaches following Yu et al. (2023), with small modifications. After washing, peaches without kernels were sliced and then dried by freeze dryers (BLK, Jiangsu BoLaiKe Refrigeration science and technology development Co., Ltd., Jiangsu, China). The freeze-dried peaches (100.00 ± 0.20 g) were completely mixed with 70 % (v/v) ethanol (5000 mL) for 2 h by a magnetic stirrer (RT, IKA, Germany). The blending process was repeated three times. Subsequently, the residue was homogenized in 3000 mL acetone for 5 min. The resulting residue (10.00 ± 0.02 g) was added to Milli-Q water (1800 mL) and kept at 100 °C for 10 min with continuously stirring by a magnetic stirrer. The residue was mixed with 900 mL of cyclohexane-trans-1,2-diamine tetra-acetic (0.05 mol/L) in potassium acetate (0.10 mol/L) for 6 h at room temperature, while the pH was adjusted to 6.5 using 0.1 mol/L HCl. Finally, the filtrate was initially dialyzed against 0.1 mol/L NaCl for 36 h followed by dialysis in Milli-Q water for additional 36 h, and then freeze-dried to obtain CSP. The detail in the structural characteristics of CSP was shown in Table S1.

2.3. SPI-CSP composites preparation

SPI solution (10 %, w/w) and CSP solutions (2 %, w/w) were prepared by mixing SPI or CSP with distilled water by a magnetic stirrer (RT, IKA, Germany) with 500 rpm at 25 °C for 2 h, respectively. SPI solution and CSP solution were homogenized with a ratio of 1:9, 3:7, 5:5, 7:3, 9:1 (w/w) by a magnetic stirrer with 500 rpm for 1 h, which were labeled as S1C9, S3C7, S5C5, S7C3, S9C1, respectively. The mixtures were treated at 90 °C for 30 min in a water bath to form the composites. The heated samples were stored at 4 °C for subsequent analyses.

2.4. Microstructure

The SEM images of the samples were captured by a microscope (ZEISS Gemini 300, ZEISS, Germany) at 3 kV accelerated voltage. Samples were coated with a thin layer of gold using an ion sputtering apparatus under a vacuum (MCI000, Hitachi Co., Ltd, Tokyo, Japan). The magnification was with 50×. The surface morphology of samples was measured by an energy dispersive X-ray spectroscopy (EDX) (Smartedx, ZEISS, Germany) at 15 kV (Mallakpour & Mohammadi, 2022).

2.5. Turbidity

Samples were firstly diluted 10 times with Milli-Q water and then the turbidity was indicated by absorbance at 600 nm at 25 °C by using a UV spectrophotometer (UV-1800, Shimadzu, Japan) (Lan, Chen, & Rao, 2018). Milli-Q water was used as a blank control.

2.6. Particle size

The size distribution of samples was determined using a laser particle size analyzer (S3500, Microtrac, USA) (Xie, Lyu, et al., 2024). After the background calibration, samples underwent triplicate measurements with 15 runs per measurement, and 10 s/run after. Detailly, D [3, 2] represented area mean diameter used to assess small particles, while D [4, 3] indicated volume mean diameter for evaluating big particles. D50 served as the median diameter, representing the particle size at 50 % cumulative frequency.

2.7. Rheological properties

The rheometer (Physica MCR301, Anton Paar, Austria) with parallel plates geometry (40 mm diameter and 1 mm gap) in frequency sweep was conducted to depict rheological properties of composites (Roque et al., 2022). We obtained the experimental flow curves through continuous shear rate from 0.01 s^{-1} to 100 s^{-1} at 25 °C. Herschel-Bulkley model Eq. (1) was applied to achieve the rheological properties at 25 °C, since samples exhibited significant yield stress (Marcotte, Taherian Hoshahili, & Ramaswamy, 2001).

$$\tau = \tau_0 + K\gamma^n \quad (1)$$

Where, K represented the flow consistency coefficient, n represented the flow behavior index, γ represented the shear rate (s^{-1}) and τ represented the shear stress (Pa).

Additionally, the storage modulus (G′) and loss modulus (G″) were determined with a fixed strain of 0.5 % at 25 °C. The procedure was conducted in the linear viscoelastic region to prevent damage to the gel structures from stress or strain (Liu, Shim, Shen, Wang, & Reaney, 2017). Power-law model Eq (2) and Eq (3) was applied to dynamic rheological properties (Tang, Roos, & Miao, 2024). Python software (Version 3.12) was used for fitting.

$$\log G' = n' \log \omega + K' \quad (2)$$

$$\log G'' = n'' \log \omega + K'' \quad (3)$$

Where, n′ and n″ represented frequency dependence indexes and ω represented the angular frequency (rad/s).

2.8. LF-NMR

The transverse relaxation time related to the moisture status was described by an LF-NMR analyzer (MiniMR-60, Suzhou Niumag Analytical Instrument Corporation, Suzhou, China) equipped with 0.5 T permanent magnet and a proton resonance frequency (23.2 MHz) at 32.00 °C. Parameters of transverse relaxation time (T_2) were set as follows: Time waiting: 2000 ms, Time echo: 0.5 ms, Number of echoes: 12,000, and Number of scans: 4. Multi-exponential model within the MultiExp Inv Analysis program was used to analyze T_2 distribution curves (Xie, Bi, et al., 2024a).

2.9. XRD and FTIR

The freeze-dried samples were characterized by an XRD diffractometer (D8 advance, Bruker, Germany) with coKα radiation (λ = 1.7889 Å) at 30 mA and 40 kV in the range from 5° to 55° (2θ). Powder ground from the freeze-dried samples were mixed with KBr (1:100, w/w) and pressed into slices to get the FTIR spectra, which was conducted on an FTIR spectrophotometer (TENSOR 27, Bruker, Germany) with a scan range from 400 to 4000 cm^{-1} at room temperature (Sun, Li, Xu, & Zhou, 2011).

2.10. Chemical forces analysis

Analysis of chemical forces were determined according to the method reported by (Ran & Yang, 2022) with slight modifications. Samples were treated by the following denaturing solutions: (1) S1, 0.05 mol/L sodium chloride solution; (2) S2, 0.6 mol/L sodium chloride solution; (3) S3, 0.6 mol/L sodium chloride solution + 1.5 mol/L urea solution; (4) S4, 0.6 mol/L sodium chloride solution + 8.0 mol/L urea solution; (5) S5, 0.5 mol/L 2-mercaptoethanol + 0.6 mol/L sodium chloride solution + 8.0 mol/L urea. To account for interference, controls and blanks were prepared for all denaturing solutions and dialysis was performed before measurement to remove β-mercaptoethanol. Composites (0.10 ± 0.02 g) were homogenized with S1, S2, S3, S4 and S5 solution (5.00 mL), respectively. After centrifuged (5000 rpm) for 10 min at 25 °C, the supernatant was collected for measuring protein content. The concentration of protein was evaluated by BSA protein concentration assay kit. In detail, the ionic bond was expressed as protein solubility dissolved in S2 and S1, hydrogen bonding was expressed as protein solubility dissolved in S3 and S2, hydrophobic interaction was expressed as protein solubility dissolved in S4 and S3, and disulfide bonding was expressed as protein solubility dissolved in S5 and S4.

2.11. 3D printing

A syringe extrusion food printer (FELIX PRO, FELIX Co. Ltd, Netherlands) was employed to print a hexagon pattern and a 21-layer cub model. The specific parameters were as follows: nozzle diameter of 1.6 mm, printing speed of 25 mm/s, 100 % infill density at room temperature. The 3D printability was assessed by printing a hexagon with an 11.4 mm filament, featuring a single-layer periphery and a three-layer center region.

2.12. Molecular docking

The molecular docking was measured by Autodock vina software (version 1.1.2, Scripps Research Institute, CA, USA), and the structure diagram was obtained by PyMol software (Version 2.5, Schrödinger company, NY, USA). Based on the CSP properties, galacturonan (galacturonic acid, CID 5459352) form Pubchem was selected as pectin model. The structures of 11 S (glycinin, PDB ID: 1FXZ) and 7 S (β-conglycinin, PDB ID:1IPK) proteins were obtained from Uniprot (Universal Protein Resource) database (Zhang et al., 2022).

2.13. Statistical analysis

All analysis were typically conducted in triplicate. Data results were presented as mean value ± standard deviation. The SPSS 19.0 (IBM, Armonk NY, USA) was used for statistical analysis of variance (ANOVA), and Duncan's multiple range tests was employed to evaluate significant differences among replicates, with statistical significance defined at $p < 0.05$. Figures were generated using Origin 9.0 software (Origin Lab Corporation, Northampton, USA).

3. Results and discussion

3.1. Appearance and microstructure

Significant stratification was observed in S1C9, S3C7, and S5C5 (with SPI: CSP mixing ratios of 1:9, 3:7 and 5:5, respectively) (Fig. 1a), indicating the phase separations accompanied with the multiphase structures. Specially, a large proportion of clear liquid was demonstrated at the top of tube of S1C9, while a small amount of white turbid liquid was found at the bottom. This could be explained by the predominant repulsive forces induced by the high concentration of CSP (Çakır & Foegeding, 2011). With the increase in SPI within the composites (e.g., S3C7 and S5C5), the clear liquid at the top of the tube became less and less, and the color of turbid liquid at the bottom became yellow. The dissociation of carboxyl groups from CSP, coupled with the formation of disordered particulate gels by SPI, enhanced the light scattering, thereby contributing to the increased turbidity observed (Archut, Drusch, & Kastner, 2022). Notably, no stratification was obtained in S7C3 and S9C1, and the homogeneous yellow color was observed. Interestingly, a significant decreased liquid level was depicted in S9C1, owing to the new formed composite with dense and network structure that could capture water.

Fig. 1b exhibited structures of SPI-CSP gels at submicron level. We could observe the relatively smooth surface of SPI, accompanied with some shallow grooves and protrusions. With the decrease in CSP concentration, the layered structure became increasingly distinct. Circle pores with varied sizes were found in S1C9. For S3C7 and S5C5, the images featured not only irregular pores but also dense grooves and protrusions. S7C3 performed a continuous and regular gel-like network structure, providing the evidence for interaction and molecular rearrangement between SPI and CSP. S9C1 displayed an extremely tight multilayer structure, which might explain the compact gel appearance and the reduced liquid level.

3.2. Particle size and turbidity

Fig. 1c showed the particle size distribution of SPI-CSP composites and SPI. As SPI bound with CSP, the particle size distribution peaks shifted significantly to left, indicating a smaller and more concentrated particle size distribution when compared to SPI. Due to the increased net charges from CSP and the resulting electrostatic repulsion between the biopolymer clusters, SPI molecules were prevented from aggregating,

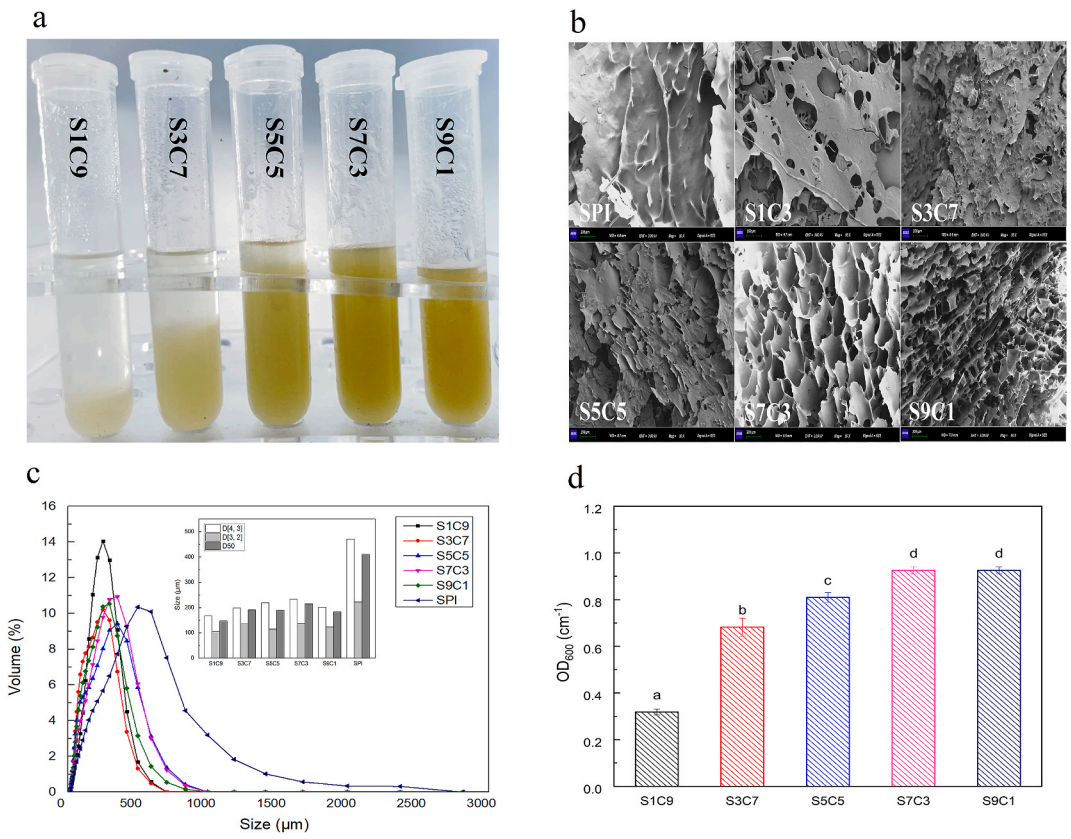

Fig. 1. Appearance (a), microstructure (b), particle size distribution (c) and turbidity (d) of SPI-CSP gels.
Note: Different lowercase letters indicate significant differences among treatments in 1d ($p < 0.05$).

leading to the small particles (He, Liu, Zhao, Li, & Wang, 2021; Yi, Gan, Wen, Fan, & Wu, 2021). The largest particle size among the SPI-CSP composites was observed in S7C3, indicating the tight aggregations. These aggregations were driven by the numerous free carboxyl groups in CSP through electrostatic interactions, as well as hydrophobic interactions between SPI and CSP (Jones & McClements, 2008). However, compared with S7C3, the tighter interactions between CSP and SPI was demonstrated in S9C1 because of the decreased particle size, which was also confirmed by SEM analysis. Due to the CSP self-aggregates, the smallest particle size (D50 = 147.9 μm) was found in S1C9, which are typically much smaller than SPI particles. No significant differences in particle size were obtained between S3C7 and S5C5, whose particle sizes were significantly higher than S1C9.

As the concentration of SPI increased, the turbidity of the composite was gradually raised (Fig. 1d). The highest turbidity (0.93) observed in S7C3 could be attributed to the formation of SPI-CSP composites, which resulted from the unfolding of SPI and the formation of SPI-pectin aggregates during the post-heating process (Lan et al., 2018). Due to its high acetylation, CSP carried abundant negative charges and offered numerous binding sites for hydrophobic interactions, contributing to the high binding ability and pectin-SPI aggregations (Lan et al., 2018). With the low CSP concentration (S7C3 and S9C1), no significant statistical differences were found. The lowest turbidity (0.31) was found in S1C9, illustrating the minimal cloudiness or haziness. Additionally, with the high CSP concentration (S1C9), the excessive pectin was dispersed in the supernatant owing to the electrostatic repulsion. With the decline in CSP concentration (such as, S3C7 and S5C5), the higher turbidity was described. This increased turbidity could be explained by the increased neutralized negative charges and the growing aggregations formed by SPI and CSP through electrostatic interactions (Sow, Toh, Wong, & Yang, 2019).

3.3. Rheological properties

3.3.1. Apparent viscosity

The apparent viscosity of SPI-CSP composites and SPI was displayed in Fig. 2a. As the shear rate increased, the apparent viscosity of all samples remarkedly decreased, illustrating their pseudoplastic characterized by shear-thinning behavior. High shear rates destroyed the structural integrity as well as the molecular chains (Zhang, Chen, & Campanella, 2024a). With the shear rate ranged from 0.01 to 100 s^{-1}, the apparent viscosities of composites dramatically dropped from 222.0000 to 0.7600 Pa s to 0.2430–0.0018 Pa s. Additionally, with the increase in SPI concentration, the apparent viscosity of the composites were notably increased, probably attributable to the thickening of SPI (Jiang et al., 2020) and the formation of new aggregates. It was worth mentioning that the viscosity of S9C1 was higher than that of SPI, which might be ascribed to the tight binding of both SPI-CSP and SPI-SPI particles in S9C1.

The shear stress was determined as a function of shear rate, and the parameters of Herschel-Bulkley model for CSP-SPI gel were summarized in Table 1. The flow behavior of CSP-SPI composites (except S9C1) was fitted well with Herschel-Bulkley model with the high coefficient of determination ($R^2 \geqq 0.90$). Meanwhile, R^2 for S9C1 was 0.8941, which was close to 0.90. The highest yield stress (τ_0) corresponded to S9C1, illustrating the greatest shear stress to initiate flow, which might be unfavorable for extrusion processes (Marcotte et al., 2001). The lower K value indicated the stronger fluidity under external force (Huang et al., 2023). As SPI increased, the K value significantly increased and then decreased, peaking at S7C3. This suggested that S7C3 had excellent stability probably owing to a strong chemical force within the composite system. Except for S1C9, n values varied from 0.6296 to 0.8329, lower than 1, confirming the non-Newtonian pseudoplastic behavior (Huang et al., 2023). Specially for S1C9, n value was greater than 1,

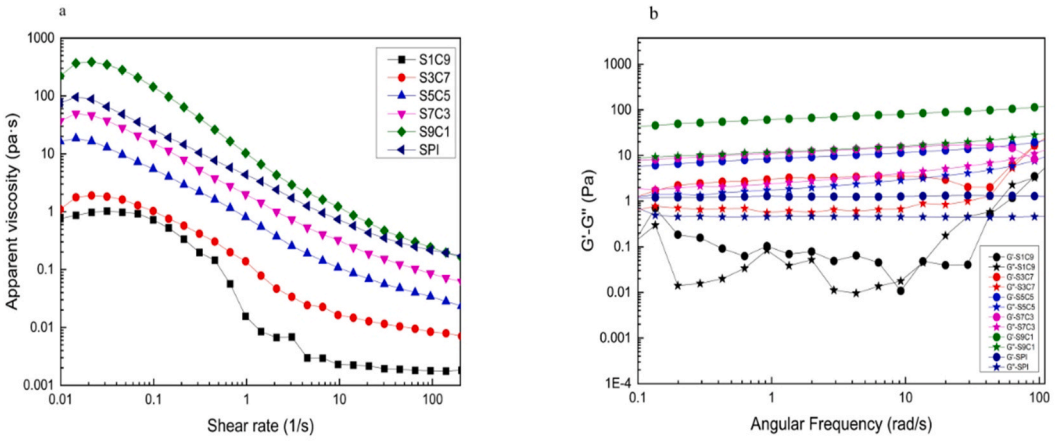

Fig. 2. Rheological properties of SPI-CSP gels: apparent viscosity (a), storage modulus (G′) and loss modulus (G″) (b).

Table 1
Rheological parameters (Herschel-Bulkley model) of SPI-CSP gels.

samples	τ_0	K	n	R^2
SPI	2.5750	0.8612	0.6773	0.9942
S1C9	0.0347	0.0003	1.3007	0.9713
S3C7	0.0784	0.0163	0.8329	0.9954
S5C5	0.4727	0.1501	0.6350	0.9935
S7C3	1.2842	0.3990	0.6296	0.9944
S9C1	10.2321	0.2703	0.8339	0.8941

demonstrating the increased viscosity with the increased shear rate, namely the dilatant behavior under shear force (Iacovino et al., 2024). Taken together, the mingling strategy of SPI and CSP enhanced the apparent viscosity and consistency index while weakened the flow index, which inflected on the facilitated viscous and shear-thinning of CSP-SPI composites.

3.3.2. *Dynamic rheological analysis*

The storage modulus (G′) and loss modulus (G″) as functions of frequency at constant strain amplitude were shown in Fig. 2b. Generally, G′ referred to the alteration in the gel network. Generally, the high G′ value displayed the enhanced gel structure. G″, as an indicator of gel viscosity, was characterized by the energy lost to viscous deformation during material deformation (Huang et al., 2024). For all samples except S1C9, within the wide range of 0.1–100 rad/s, G′ was higher than G″ suggesting that these samples could be considered as the gel system (Ji, Xue, Zhang, Li, & Xue, 2017). For S1C9, under the low angular frequency (0.1–10 rad/s), G′ was significantly higher than G″, suggesting the viscous-dominated behavior. As the angular frequency increased to the higher range (10–100 rad/s), G″ gradually approached G′ and eventually higher than G″. This changed behavior indicated the transition from elastic to viscous behavior (gel/sol transition) associated with Ca^{2+}-mediated pectin gel (Zhao et al., 2024). The rheological behavior of S1C9 could be ascribed to the electrostatic interference among the multiple particles, such as CSP-CSP, SPI-SPI and SPI-CSP aggregates. Moreover, G′ and G″ of SPI were smaller than that of S3C7, S5C5, S7C3 and S9C1, which was driven by the denaturation and unfolding of SPI and the interaction between SPI and CSP. The enhancement in G′ and G″ suggested that the conjugation of protein and pectin might absorb excess moisture through hydrogen bonding. Additionally, CSP homogenously distributed within SPI gel network structure, which provided direct evidence of the improved gel properties accompanied with the increased G′ and G″ values (Huang et al., 2024; Rios et al., 2024). Additionally, the highest G′ and G″ were shown in S9C1, followed by S7C3, indicating the great gel strength in S9C1. This improved gel strength that reflected by the firm structure was ascribed to the strong interaction between SPI and CSP.

Based on the excellent dynamic rheological properties, the structure properties of S7C3 and S9C1 were further analyzed by Power-law model, the relationship of G′ and G″ between angular frequency (0.0628–92.2 rad/s) was also explored. Additionally, the gel characteristic of the SPI-CSP were described based on the parameters K′, K″, n′, and n″ (Ge et al., 2023) (Table 2). Gels can be classified into physical gels, entanglement network gels (EN gels), and covalently cross-linked gels (CC gels) (Ge et al., 2023; Tunick, 2011). Generally, CC gels, considered the strong gels, were characterized by a permanent network of covalent bonds, with G′ being almost independent of frequency (ideally $n' = 0$) (Tang et al., 2024). In contrast, EN gels featured strong G′ frequency independence and even the G′-G″ crossover points, indicating the transition from viscous (fluid-like) to elastic (solid-like) behavior (Gunasekaran & Ak, 2000; Tang et al., 2024). The low correlation coefficients ($n' = 0.095$ for G′ and $n'' = 0.091$ for G″), close to 0, along with the high storage and loss moduli in S9C1, indicated the properties of a CC gel. This result was corroborated well with SPI-gum gel with stable structure and strong elasticity and viscosity (Chang, Li, Wang, Bi, & Adhikari, 2014). Additionally, the high storage modulus (G′) and the reduced frequency dependence of S9C1 demonstrated the strong temporal stability accompanied by the rigid gel network formed by the stable covalent bonds within the gel matrix (Tang et al., 2024). Owing to the high SPI content in S9C1, the cross-linking between protein molecular was significantly enhanced by the post-heat processing, which further promoted the protein-protein interactions (including disulfide bonds) to form the stable covalent bonds and resulted in a rigid gel network. Unlike S9C1, alongside the intersected G′ and G″, both the low n′ (0.094) and high n″ (0.233) in S7C3 demonstrated the typical properties of an EN gel, namely, the good mechanical properties under high frequencies and the flexible network structure at low frequencies (Gunasekaran and Ak, 2000; Moreno et al., 2020; Tang et al., 2024). Since the appropriate mingling ratio of SPI and CSP, the well-calculated physical entanglements and hydrogen bonds might contribute to the reversible non-covalent interactions, which contributed to the high-frequency dependence and good elasticity of S7C3. Furthermore, compared with S7C3, the higher K′ and K″ in S9C1 indicated the strengthened elasticity and viscosity, reflecting the greater gel rigidity and firmness, which

Table 2
Rheological parameters (Power-law model) of SPI-CSP gels.

samples	$\log G' = n' \log \omega + K'$			samples	$\log G'' = n'' \log \omega + K''$		
	n′	k’	R^2		n″	k″	R^2
S7C3	0.094	1.032	0.858	S7C3	0.223	0.427	0.935
S9C1	0.095	1.779	0.995	S9C1	0.091	1.082	0.972

provided great resistance to deformation (Moreno et al., 2020). It was reasonable to conclude that the distinct rheological behaviors observed in S9C1 and S7C3 should be attributed to the differences in their gel network structures and interaction forces.

3.4. Elemental distribution

SEM-EDX has been widely used for precisely characterizing the surface morphology, elemental localization, elemental composition and atomic percentage of materials (Bakeshlouy Afshar, Poursattar Marjani, & Gozali Balkanloo, 2024). Fig. 3 showed the elemental distribution within SPI and SPI-CSP gels. The atomic percentages of the identified elements, namely Carbon (C), Nitrogen (N), Oxygen (O), Phosphorus (P), Sulfur (S), and Calcium (Ca), were presented in Table 3. For SPI, all elements were homogeneously distributed within the smooth regions. Conversely, the element mapping of SPI-CSP composites exhibited non-uniform distributions. Specifically, the high intensity signals of C and O were observed in all samples. C had the highest atomic percentage, signifying that C was the dominant component in these samples. With the increase in CSP concentration, the atomic percentage of O gradually decreased. The big atomic percentage of O in S1C9 (33.31 %) further indicated the distribution of pectin within the composite. Additionally, the distribution of C, O, and N was tightly concentrated in SPI-CSP samples, highlighting that the backbone structure of these gels was primarily composed by closely linked C, O, and N. This observation indicated that electrophilic carbonyl groups from CSP entangled with neutral amino acids from SPI through covalent bonds, which was beneficial for forming the SPI-CSP gels (de Oliveira, Coimbra, de Oliveira, Zuñiga, & Rojas, 2016; Zhang et al., 2019). S, being a distinctive element in protein, was utilized to track the changes in the structure of SPI. With increasing SPI concentration, S tended to concentrate in specific regions, which performed the degree of protein aggregation. As in S1C9, S3C7, and S5C5 (Fig. 3b–d), we observed the uniform distribution of S. However, as for S7C3 and S9C1 (Fig. 3e and f), the distribution of S with less homogeneity but high percentage was observed, which elucidated the formation of SPI-CSP gel structure through strong intermolecular force between SPI and CSP. Additionally, the increased P and Ca in S7C3 and S9C1 might contribute to the formation of P/Ca bridges within the gels, which could enhance the rigidity and stability (Xie, Bi, et al., 2024a). S9C1 exhibited the highest Ca percentage (15 %), which was aligned with the biggest viscosity, G′ and G″.

Table 3
Atomic percentage of SPI-CSP gels.

elements	atomic percentage (%)					
	S1C9	S3C7	S5C5	S7C3	S9C1	SPI
C	61.3	57.51	58.5	62.96	62.45	63.59
N	5.11	13.28	12.91	12.46	15.27	14.62
O	33.31	28.73	27.99	23.24	20.95	21.23
P	0.15	0.23	0.32	0.66	0.63	0.28
S	0.09	0.23	0.25	0.60	0.55	0.21
Ca	0.04	0.03	0.03	0.08	0.15	0.06

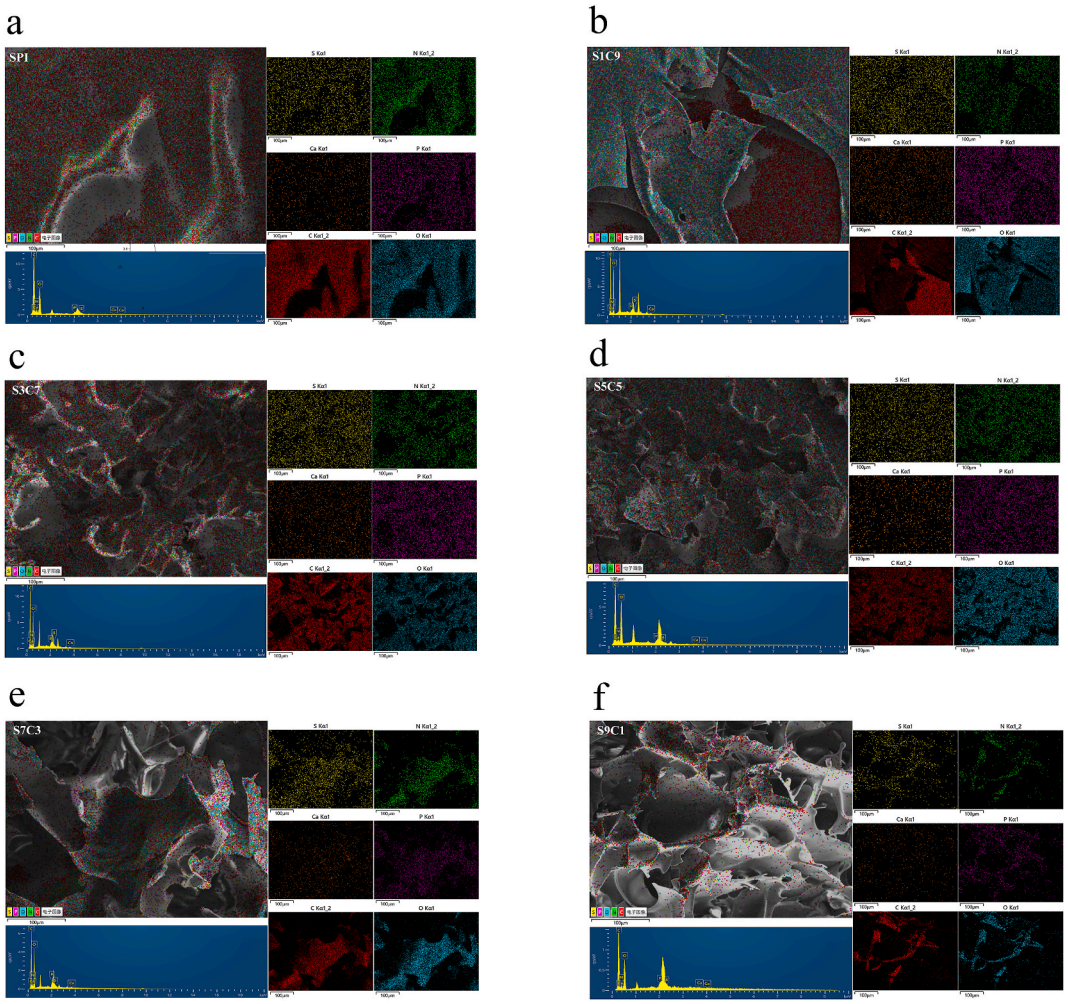

Fig. 3. Scanning electron microscopy with energy dispersive x-ray spectroscopy (SEM-EDX) images of SPI-CSP gels.

3.5. LF-NMR

LF-NMR has been widely applied to describe the water content, water distribution, and interactions between water and biomolecules within gel systems, which provided a clear insight into intramolecular interactions among functional groups (Huang et al., 2024). Generally, the spin-spin relaxation times (T_2) in LF-NMR reflected the proton rotational mobility. A shorter T_2 value indicated the faster decay and stronger interactions with hydrogen protons, while a longer T_2 value suggested the enhanced water mobility within the matrix (Wang, Zhang, Bhandari, & Gao, 2016). The relaxation times of the peaks were categorized into T_{21}, T_{22}, and T_{23}. In detail, T_{21}, representing bound water, was associated with water molecules tightly bounded to amino and carbonyl groups through hydrogen bonding. T_{22} was further divided into T_{22a} and T_{22b}, both linked to immobilized water, and T_{23} was indicative of free water (Moller et al., 2011). As shown in Table 4, free water (T_{23}) was the predominant water in gels, accounting for 94.33–98.33 %. The longest T_{23} demonstrating the highest hydration levels was exhibited in S1C9, which suggested the weak water holding capacity when subjected to external force. Conversely, the shortest T_{23} assigned to the lowest fluidity was revealed in S9C1, suggesting the strong water holding capacity (Luo et al., 2020). Except for S9C1, T_{22} displayed two distinct peaks (T_{22a} and T_{22b}) in SPI-CSP gels, illustrating the heterogeneity of moisture molecular resulted from the varied interactions among the components within the gel matrix. The shortest T_{22a} was displayed in S7C3, followed by S9C1, suggesting the reduced mobility of moisture induced by the formation of numerous SPI-CSP aggregates (Luo et al., 2020). Regarding T_{22b}, S1C9 had the largest area proportion (4.63 %), illustrating the excellent capacity for capturing water molecular within the network structure of gels. CSP, acting as a low methoxyl pectin, could trap water through Ca bridges within its dense structure, (Ca sourced from SPI). Additionally, under heating actions, low methoxyl pectin could form a compact gel structure to secure water based on the "egg-box model" (Gawkowska, Cybulska, & Zdunek, 2018). No significant T_{21} was achieved in SPI. Interestingly, subjecting to CSP addition, the signal of T_{21} was detected in all SPI-CSP gels. A potential explanation for the detected T_{21} was the captured water molecular, by SPI-CSP network structure (Fu et al., 2023). The shortest T_{21} was observed in S9C1, suggesting the strong water-binding capacity. Especially, both S7C3 and S9C1 exhibited the highest M_{21} values (0.82 %), indicating the lowest mobility of water, which might be ascribed to the strong bonding interactions between moisture molecular and biomacromolecules by hydrogen bonds (Fu et al., 2023).

3.6. XRD

The XRD resulting diffraction patterns provided the valuable information regarding the average size, degree of crystallinity, and different phases of the material. In the case of typical crystalline structures, the XRD curve would exhibit sharp peaks, whereas amorphous materials would produce smooth and broad spectrum (Bakeshlouy Afshar et al., 2024). Fig. 4a showed the XRD spectra of CSP, SPI and SPI-CSP composites. For CSP, three intense peaks were observed at 8.37°, 15.29°, and 22.34°, respectively, which illustrated crystalline properties of CSP. Two characteristic peaks with the wide ranges at 8.82° and 19.90°were found in SPI, indicating the partially crystalline state. There were two distinct peaks in S1C9, namely, one peak was at 8.31°, which was similar to the peak (8.37°) obtained in CSP, identifying the presence of pectin aggregation. The other wide peak located at 22.89°, revealing the formation of the new hypocrystalline composite (Kang et al., 2022). With the increase in the content of SPI, the peaks of SPI-CSP gels varied from 19° to 23° were left-shifted accompanied with the increased intensity, which reflected the altered crystalline characteristics. The most pronounced peak (19.25°) was quantified in S9C1 assigned to the enhanced interactions between SPI and CSP, demonstrating the most ordered crystalline structures. Conversely, the smoothest peak (22.38°) in S3C7 depicted the less ordered structure and the weak crystalline properties (Jiang et al., 2021).

3.7. FT-IR

The changes in the polymer conditions and interpretations of SPI, CSP, and SPI-CSP gels were performed by FTIR analysis (Fig. 4b). The excellent compatibility between SPI and CSP was reflected on the spectra of SPI-CSP gels, indicating the stable chemical composition within the composites matrix (Bakeshlouy Afshar et al., 2024). A clear characteristic peak around 3450 cm^{-1} associated with O-H stretching was attributed to the glucopyranose rings in polysaccharides. The peak at 2930 cm^{-1} was corresponded to C-H asymmetric stretching vibration. The peaks around 1640 cm^{-1}, relating to the changes in O-H conformation, indicated the entrance of water molecules into the pectin structure (Bakeshlouy Afshar et al., 2024). Peaks around 1410 cm^{-1} were associated with the bending vibrations of C-H in -CH_2 and -OH groups (Bakeshlouy Afshar et al., 2024). The absorption peak around 1035 $cm^{-1}$was assigned to the stretching vibration of the C-O and C-C bond, moreover the bending vibration of C-OH. A small characteristic peak at 920 cm^{-1} was assigned to the -OH bond (Marzieh Bakeshlouy Afshar et al., 2024).

Following the mingling strategy, the absorption bands around 3700 - 3480 cm^{-1} in composites, assigned to O-H stretching, became broader and shifted to lower wavelengths compared to the 3460 cm^{-1} absorption peak in SPI, suggesting strengthened hydrogen bonds (Ran and Yang, 2022). Several new characteristic peaks around 1658 cm^{-1} assigned to C=N stretching vibration were presented in SPI-CSP gels, confirming the formation of new aggregations (Ma et al., 2020). Compared with SPI, the absorption bands in SPI-CSP (particularly for S7C3 and S9C1) related to amide I (1590–1710 cm^{-1}) and amide II (1490–1590 cm^{-1}) shifted to lower wavelengths, indicating the regular network structure (Ran and Yang, 2022). Furthermore, subjecting to CSP addition, the intensity of absorption peak at 1530 cm^{-1} attributed to -NH_2 groups was significantly decreased, which illustrated that -NH_2 groups participated in the aggregation process and formed new substances. Additionally, compared with CSP, the peaks for SPI-CSP gels in the range of 1400–1200 cm^{-1} were smoother, which also confirmed the formation of new aggregations. Besides, the special fingerprint region of CSP was also exhibited in S1C9, which also supported the pectin aggregations.

3.8. Chemical force

Changes in protein structure during gel processing could

Table 4
Water distribution in LF-NMR of SPI-CSP gels.

	T_{21} (ms)	M_{21} (%)	T_{22a} (ms)	M_{22a} (%)	T_{22b} (ms)	M_{22b} (%)	T_{23} (ms)	M_{23} (%)
SPI	\		1.60	0.33	7.84	1.03	166.38	98.65
S1C9	0.95	0.54	18.04	0.39	235.43	4.63	1431.46	94.33
S3C7	0.91	0.78	14.65	0.30	72.33	2.53	310.79	96.39
S5C5	0.98	0.80	4.90	0.28	31.44	0.90	410.27	98.02
S7C3	0.98	0.82	3.18	0.11	12.75	0.74	333.13	98.33
S9C1	0.79	0.82	4.82	0.89	\	\	191.16	98.29

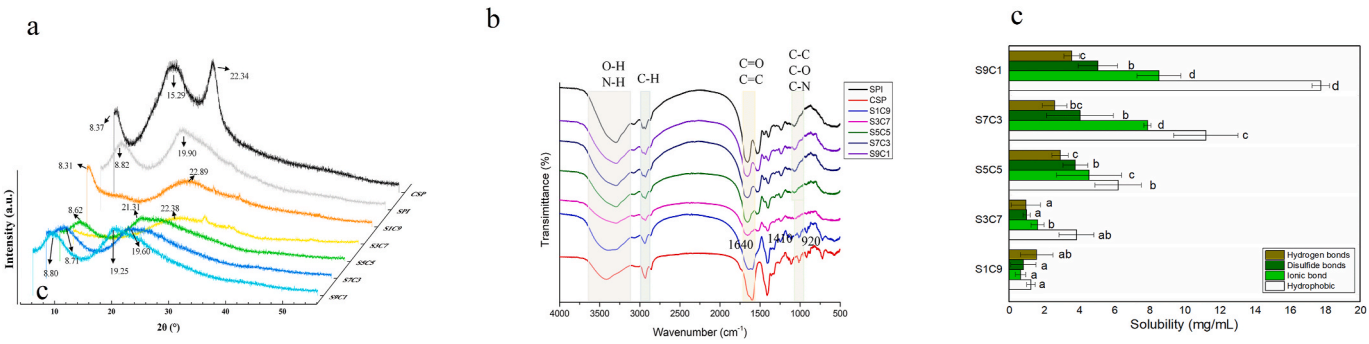

Fig. 4. X-ray diffraction (XRD) patterns (a), FT-IR spectra (b) and chemical forces analysis (c).
Note: Different lowercase letters indicate significant differences among treatments in Fig. 3c ($p < 0.05$).

significantly affect the interaction among molecules within the matrix, which would in turn have crucial effects on gelation properties. Typically, NaCl could disrupt electrostatic interactions, while urea served as an effective hydrogen bonds and hydrophobic interactions breaker. Additionally, 2-mercaptoethanol was used to break disulfide bonds (Nakauma et al., 2017; Ran and Yang, 2022; Wang et al., 2018). As shown in Fig. 4c, except for S1C9, hydrophobic interaction was significantly higher than hydrogen bond, disulfide bond and ionic bond. Detailly, S9C1 displayed the highest of hydrophobic interaction (17.66 mg/mL) and ionic bond (8.55 mg/mL), which were beneficial for the stable network of gel (Ran and Yang, 2022). With the increase in SPI concentration accompanied with amount of hydrophobic groups, aggregates were more easily be formed, which facilitated the possible release of water molecules into the gel's system, thereby increasing the system's overall entropy (Krimm, 1980; Rangel-Yagui, Pessoa-Jr, & Blankschtein, 2004). Following the mingling strategy of SPI and CSP, these four types of interactions were intensified as well as the enhanced gel strength. Specially, CSP with low methoxyl could contribute to the salt bridges through "pectin-Ca-protein cross-linking" within SPI-CSP gels, which enhanced the ionic bond (Wang et al., 2018). As differed from other test groups, hydrogen bond was the predominant chemical force in S1C9, owing to the amount of CSP aggregates in S1C9. This was also confirmed in the analysis of particle size and FTIR.

3.9. Printability

Based on the analysis of physio-chemical features and the rheological properties, S7C3 and S9C1 were selected as the suitable food inks for 3D printing. As observed in the printing geometries (Fig. 5), SPI could not be continuously and uniformly extruded out from the nozzle. The slight collapse and the poor layer stacking were observed in SPI gel, indicating poor stability. This phenomenon could be explained by the poor mechanical strength and disordered network system confirmed by the low G′ and G″ and the micro-structure of SPI (Phuhongsung, Zhang, & Devahastin, 2020). S7C3 and S9C1 exhibited integrated structures. As proven from the enhanced rheology properties, the entanglement between CSP and SPI reduced the overlap and spatial repulsion within the composite matrix, contributing to the regular network structure, which was preferred for the deposited layers and holding the printed structures (Wang et al., 2024a, 2024b). However, it was difficult for S9C1 to extrude out from the nozzle to from the regular shape during the printing process, due to the dense and robust microstructure. Thus, S9C1, with its low flowability and poor printing performance, showed a rough surface and inferior cohesive interlayer structure as well as visible granular and separated areas. S7C3 with excellent viscosity (e.g., high G′) was easily extruded out from the nozzle and fluently printed the 3D pattern with the special shape contours and smooth surface and without any obvious sticking and collapse. Apparently, the uniform and regular layered structure with excellent interlayer adhesion was displayed in S7C3, demonstrating exceptional printability. When subjected to strong external pressure, S7C3 tended to be in a fluid-like state (favorable for extrusion), conversely, without external pressure, S7C3 returned to the solid-like state (Gunasekaran and Ak, 2000; Tang et al., 2024). Specially, the balanced hydrogen bond and hydrophobic interaction within the S7C3 system showed direct evidence of the flexible gel network and the enhanced 3D printability. In contrast, the intense SPI-SPI interaction and hydrophobic interaction within the S9C1 system led to serious aggregation, which was reflected in the reduced flowability (shown in T_2 (Table 4)) and clogging during extrusion. It was reasonable to conclude that the mingling strategy, including SPI and CSP with the appropriate concentration (such as S7C3), could induce the enhanced mechanical strength and the excellent rheological properties, which was conducive to completed the fusion between the layers and maintain the shape-fidelity of 3D printed objects with the accuracy and quality (Phuhongsung et al., 2020) (see Fig. 6).

3.10. Formation mechanism of SPI-CSP composites

As the consequence of the analysis of macro- & micro-morphology, physio-chemical properties, internal function group and chemical

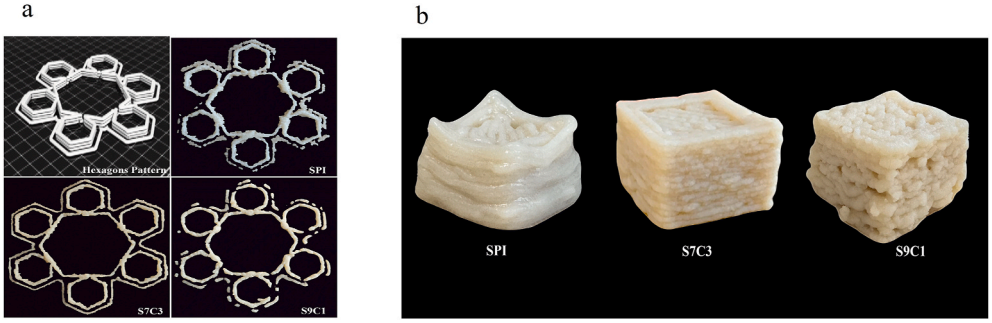

Fig. 5. Hexagons pattern (a) and 21-layer cube (b) 3D-printing results of SPI and SPI-CSP gels.

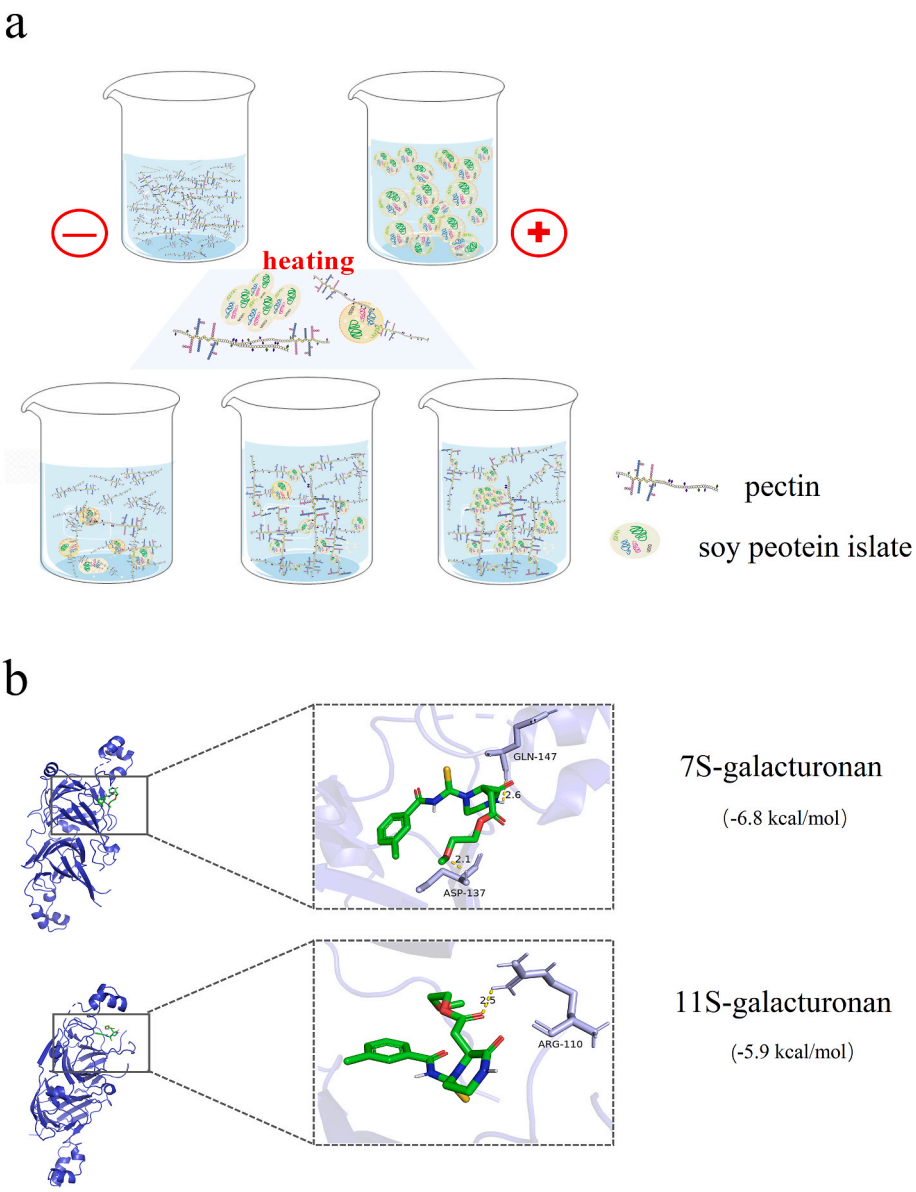

Fig. 6. Interaction models (a) and molecular docking analysis (b) between SPI and CSP.

force, we believed that SPI strongly interacted with CSP within the composite matrix. When the abundance negative charges (mainly from CSP) were dominant, the strengthened molecular repulsion would lead to phase separation and the biphasic solution (e.g., S1C9). Alongside the appropriate mixing ratio, the homogeneous phase was observed in S7C3, probably because of electrostatic interactions caused by the similar amounts of negative charges from CSP and positive charges from SPI. However, as SPI concentration further increased (S9C1), the SPI self-aggregation was dominant within the composite matrix, which contributed to the decreased gel properties. Alongside the binding between protein and pectin, water molecules within the matrix were released into the solution. The release of water molecules led to an increase in the system's entropy, which in turn resulted in a decreased system's free energy (Krimm, 1980; Rangel-Yagui et al., 2004). As the decrease in the free energy of the composite system, the soluble composites further aggregated and precipitated. Moreover, the changes in structures of SPI and CSP deeply induced by the post-heating action could promote the interaction between SPI and CSP, which further resulted in the formation of new composites (Fig. 5a). Therefore, the primary binding modalities between CSP and SPI were explored by molecular docking, in which galacturonan ligand and 7 S (β-conglycinin) and 11 S (glycinin) were selected as the structural domains of CSP and SPI, respectively (Zhang et al., 2022). As shown in Fig. 5b, the negative binding affinity energies indicated the potential for stable binding (Zhang et al., 2022). For the β-conglycinin, the active amino acid sites ASP-137 and GLN-147 should be considered as the key interactions with 2.1 Å and 2.6 Å bond distance, respectively. The best binding site of galacturonan to glycinin was identified in ARG-110, with a bond distance of 2.5 Å. The binding energy of galacturonan to β-conglycinin was −6.8 kcal/mol, which was lower than the binding energy to glycinin (−5.9 kcal/mol). This lower binding energy should be explained by the stable hydrogen bonds and electrostatic interactions. Additionally, galacturonan was more readily bound to 7 S than to 11 S, implying 7 S might have a stronger potential to stabilize the gel structure.

4. Conclusion

This study comprehensively analyzed the effects of mingling strategy of SPI and CSP at the various concentrations on the rheological,

structural, and functional properties of SPI-CSP composites, with a focus on their potential as food inks for 3D printing. Our findings revealed that increasing SPI concentrations enhance particle distribution, viscosity, viscoelastic properties (G′ and G″), water-holding capacity, and overall gel strength. Notably, S9C1 formed covalently CC gels, while S7C3 illustrated the properties of EN gels. The formation of new SPI-CSP composites was confirmed by FT-IR, XRD, and SEM-EDX analyses, highlighting the molecular interactions between SPI and CSP. Hydrophobic interactions and ionic bonding were identified as key chemical force in formation of stable and robust gel structures. Molecular docking further suggested that β-conglycinin (7 S) plays a more significant role in stabilizing the gel structure than glycinin (11 S). Among the formulations, S7C3, with excellent viscosity, mechanical strength, and rheological properties was identified as the optimal food ink for 3D printing, which could produce the high-precision printed structure with smooth surfaces and stable shapes. These findings provide valuable insights into the development of 3D printing food inks, offering a pathway to developing customizable, nutrient-rich, and structurally robust food products, which have the potential to meet the needs of individuals with specific dietary requirements, including those with difficulty chewing or swallowing, or those requiring high-protein diets.

CRediT authorship contribution statement

Jin Xie: Writing – review & editing, Writing – original draft, Visualization, Methodology, Investigation, Data curation, Conceptualization. **Jinfeng Bi:** Supervision, Project administration. **Xiaoxian Liu:** Writing – review & editing, Data curation. **Christophe Blecker:** Visualization, Formal analysis. **Nicolas Jacquet:** Writing – review & editing, Supervision. **Jian Lyu:** Writing – review & editing, Supervision, Project administration, Funding acquisition.

Declaration of competing interest

The authors declared that they have no conflicts of interest to this work. We declare that we do not have any commercial or associative interest that represents a conflict of interest in connection with the work submitted.

Acknowledgments

The research was supported by the National Key Research and Development Plan (2022YFD1600704) and China Scholarship Council (202203250073).

Appendix A. Supplementary data

Supplementary data to this article can be found online at https://doi.org/10.1016/j.foodhyd.2024.110904.

Data availability

Data will be made available on request.

References

Ahmadi Soufivand, A., Faber, J., Hinrichsen, J., & Budday, S. (2023). Multilayer 3D bioprinting and complex mechanical properties of alginate-gelatin mesostructures. *Scientific Reports, 13*(1), Article 11253. https://doi.org/10.1038/s41598-023-38323-2

Archut, A., Drusch, S., & Kastner, H. (2022). Complex coacervation of pea protein and pectin: Effect of degree and pattern of free carboxyl groups on biopolymer interaction. *Food Hydrocolloids, 133*, Article 107884. https://doi.org/10.1016/j.foodhyd.2022.107884

Bakeshlouy Afshar, M., Poursattar Marjani, A., & Gozali Balkanloo, P. (2024). Introducing graphene quantum dots in decomposable wheat starch-gelatin based nano-biofilms. *Scientific Reports, 14*(1), 2069. https://doi.org/10.1038/s41598-024-52560-z

Bi, A.-Q., Xu, X.-B., Guo, Y., Du, M., Yu, C.-P., & Wu, C. (2022). Fabrication of flavour oil high internal phase emulsions by casein/pectin hybrid particles: 3D printing performance. *Food Chemistry, 371*, 131349.

Çakır, E., & Foegeding, E. A. (2011). Combining protein micro-phase separation and protein–polysaccharide segregative phase separation to produce gel structures. *Food Hydrocolloids, 25*(6), 1538–1546. https://doi.org/10.1016/j.foodhyd.2011.02.002

Chang, Y. Y., Li, D., Wang, L. J., Bi, C. H., & Adhikari, B. (2014). Effect of gums on the rheological characteristics and microstructure of acid-induced SPI-gum mixed gels. *Carbohydrate Polymers, 108*, 183–191. https://doi.org/10.1016/j.carbpol.2014.02.089

Chen, J., Sun, H., Mu, T., Blecker, C., Richel, A., Richard, G., et al. (2022). Effect of temperature on rheological, structural, and textural properties of soy protein isolate pastes for 3D food printing. *Journal of Food Engineering, 323*, Article 110917. https://doi.org/10.1016/j.jfoodeng.2021.110917

de Oliveira, F. C., Coimbra, J. S., de Oliveira, E. B., Zuñiga, A. D., & Rojas, E. E. (2016). Food protein-polysaccharide conjugates obtained via the maillard reaction: A review. *Critical Reviews in Food Science and Nutrition, 56*(7), 1108–1125. https://doi.org/10.1080/10408398.2012.755669

Feng, M., Zhang, M., Mujumdar, A. S., & Guo, Z. (2024). Influence of components interaction in recombined food gels on 3D printing: A comprehensive review. *Food Hydrocolloids, 151*, Article 109782. https://doi.org/10.1016/j.foodhyd.2024.109782

Fu, H., Li, J., Yang, X., Swallah, M. S., Gong, H., Ji, L., et al. (2023). The heated-induced gelation of soy protein isolate at subunit level: Exploring the impacts of α and α′ subunits on SPI gelation based on natural hybrid breeding varieties. *Food Hydrocolloids, 134*, Article 108008. https://doi.org/10.1016/j.foodhyd.2022.108008

Gawkowska, D., Cybulska, J., & Zdunek, A. (2018). Structure-related gelling of pectins and linking with other natural compounds: A review. *Polymers, 10*(7), 762. https://doi.org/10.3390/polym10070762

Ge, J., Sun, C., Chang, Y., Li, S., Zhang, Y., & Fang, Y. (2023). Understanding the differences in heat-induced gel properties of twelve legume proteins: A comparative study. *Food Research International, 163*, Article 112134. https://doi.org/10.1016/j.foodres.2022.112134

Gu, M., Gu, H., Raghavan, V., & Wang, J. (2024). Ultrasound treatment improved the physicochemical properties of pea protein with pectin ink used for 3D printing. *Future Foods, 9*, 100377. https://doi.org/10.1016/j.fufo.2024.100377.

Gunasekaran, S., & Ak, M. M. (2000). Dynamic oscillatory shear testing of foods — selected applications. *Trends in Food Science & Technology, 11*(3), 115–127. https://doi.org/10.1016/S0924-2244(00)00058-3

He, Z., Liu, C., Zhao, J., Li, W., & Wang, Y. (2021). Physicochemical properties of a ginkgo seed protein-pectin composite gel. *Food Hydrocolloids, 118*, 106781. https://doi.org/10.1016/j.foodhyd.2021.106781.

Huang, C., Blecker, C., Wei, X., Xie, X., Li, S., Chen, L., et al. (2024). Effects of different plant polysaccharides as fat substitutes on the gel properties, microstructure and digestion characteristics of myofibrillar protein. *Food Hydrocolloids, 150*, Article 109717. https://doi.org/10.1016/j.foodhyd.2023.109717

Huang, G., Liu, G., Xu, Z., Jiang, L., Zhang, Y., & Sui, X. (2023). Stability, rheological behavior and microstructure of Pickering emulsions co-stabilized by soy protein and carboxymethyl chitosan. *Food Hydrocolloids, 142*, Article 108773. https://doi.org/10.1016/j.foodhyd.2023.108773

Iacovino, S., Trivisonno, M. C., Messia, M. C., Cuomo, F., Lopez, F., & Marconi, E. (2024). Combination of empirical and fundamental rheology for the characterization of dough from wheat flours with different extraction rate. *Food Hydrocolloids, 148*, Article 109446. https://doi.org/10.1016/j.foodhyd.2023.109446

Ji, L., Xue, Y., Zhang, T., Li, Z., & Xue, C. (2017). The effects of microwave processing on the structure and various quality parameters of Alaska pollock surimi protein-polysaccharide gels. *Food Hydrocolloids, 63*, 77–84. https://doi.org/10.1016/j.foodhyd.2016.08.011

Jiang, L., Zhang, J., Ren, Y., Shen, M., Yu, Q., Chen, Y., et al. (2021). Acid/alkali shifting of Mesona chinensis polysaccharide-whey protein isolate gels: Characterization and formation mechanism. *Food Chemistry, 355*, Article 129650. https://doi.org/10.1016/j.foodchem.2021.129650

Jiang, Q., Zhao, S., Zhao, W., Wang, P., Qin, P., Wang, J., et al. (2024). The role of water distribution, cell wall polysaccharides, and microstructure on radish (Raphanus sativus L.) textural properties during dry-salting process. *Food Chemistry X, 22*, Article 101407. https://doi.org/10.1016/j.fochx.2024.101407

Jones, O. G., & McClements, D. J. (2008). Stability of biopolymer particles formed by heat treatment of β-lactoglobulin/Beet pectin electrostatic complexes. *Food Biophysics, 3*(2), 191–197. https://doi.org/10.1007/s11483-008-9068-5

Kang, X., Jia, S., Gao, W., Wang, B., Zhang, X., Tian, Y., et al. (2022). The formation of starch-lipid complexes by microwave heating. *Food Chemistry, 382*, Article 132319. https://doi.org/10.1016/j.foodchem.2022.132319

Krimm, S. (1980). The hydrophobic effect: Formation of micelles and biological membranes. *Journal of Polymer Science: Polymer Letters Edition, 18*(10), 687. https://doi.org/10.1002/pol.1980.130181008, 687.

Lan, Y., Chen, B., & Rao, J. (2018). Pea protein isolate–high methoxyl pectin soluble complexes for improving pea protein functionality: Effect of pH, biopolymer ratio and concentrations. *Food Hydrocolloids, 80*, 245–253. https://doi.org/10.1016/j.foodhyd.2018.02.021

Liu, J., Shim, Y. Y., Shen, J., Wang, Y., & Reaney, M. J. T. (2017). Whey protein isolate and flaxseed (Linum usitatissimum L.) gum electrostatic coacervates: Turbidity and rheology. *Food Hydrocolloids, 64*, 18–27. https://doi.org/10.1016/j.foodhyd.2016.10.006

Luo, H., Guo, C., Lin, L., Si, Y., Gao, X., Xu, D., et al. (2020). Combined use of rheology, LF-NMR, and MRI for characterizing the gel properties of hairtail surimi with potato

starch. *Food and Bioprocess Technology, 13*(4), 637–647. https://doi.org/10.1007/s11947-020-02423-y

Ma, X., Chen, W., Yan, T., Wang, D., Hou, F., Miao, S., et al. (2020). Comparison of citrus pectin and apple pectin in conjugation with soy protein isolate (SPI) under controlled dry-heating conditions. *Food Chemistry, 309*, Article 125501. https://doi.org/10.1016/j.foodchem.2019.125501

Mallakpour, S., & Mohammadi, N. (2022). Development of sodium alginate-pectin/TiO (2) nanocomposites: Antibacterial and bioactivity investigations. *Carbohydrate Polymers, 285*, Article 119226. https://doi.org/10.1016/j.carbpol.2022.119226

Marcotte, M., Taherian Hoshahili, A. R., & Ramaswamy, H. S. (2001). Rheological properties of selected hydrocolloids as a function of concentration and temperature. *Food Research International, 34*(8), 695–703. https://doi.org/10.1016/S0963-9969(01)00091-6

Moller, S. M., Grossi, A., Christensen, M., Orlien, V., Soltoft-Jensen, J., Straadt, I. K., et al. (2011). Water properties and structure of pork sausages as affected by high-pressure processing and addition of carrot fibre. *Meat Science, 87*(4), 387–393. https://doi.org/10.1016/j.meatsci.2010.11.016

Moreno, H. M., Domínguez-Timón, F., Díaz, M. T., Pedrosa, M. M., Borderías, A. J., & Tovar, C. A. (2020). Evaluation of gels made with different commercial pea protein isolate: Rheological, structural and functional properties. *Food Hydrocolloids, 99*, Article 105375. https://doi.org/10.1016/j.foodhyd.2019.1053

Nakauma, M., Funami, T., Fang, Y., Nishinari, K., Draget, K. I., & Phillips, G. O. (2017). Calcium binding and calcium-induced gelation of normal low-methoxyl pectin modified by low molecular-weight polyuronate fraction. *Food Hydrocolloids, 69*, 318–328. https://doi.org/10.1016/j.foodhyd.2016.12.035

Phuhongsung, P., Zhang, M., & Devahastin, S. (2020). Investigation on 3D printing ability of soybean protein isolate gels and correlations with their rheological and textural properties via LF-NMR spectroscopic characteristics. *Lwt, 122*, Article 109109. https://doi.org/10.1016/j.lwt.2020.109019

Ran, X., & Yang, H. (2022). Promoted strain-hardening and crystallinity of a soy protein-konjac glucomannan complex gel by konjac glucomannan. *Food Hydrocolloids, 133*, Article 107959. https://doi.org/10.1016/j.foodhyd.2022.107959

Rangel-Yagui, C. O., Pessoa-Jr, A., & Blankschtein, D. (2004). Two-phase aqueous micellar systems: An alternative method for protein purification. *Biotechnology, 21*, 531–544. https://doi.org/10.1590/S0104-66322004000400003

Rios, W. V., Geonzon, L. C., Roque, A. M., Abiquibil, M. R. B., Pilapil, M. D. A., Lingaro, M. A. P., et al. (2024). The effects of stem bromelain on the gelation behavior of kappa carrageenan under linear and nonlinear rheological regimes. *Food Hydrocolloids, 150*, Article 109662. https://doi.org/10.1016/j.foodhyd.2023.109662

Roque, A. M., Montinola, D., Geonzon, L., Matsukawa, S., Lobarbio, C. F. Y., Taboada, E. B., et al. (2022). Rheological elucidation of the viscoelastic properties and network interaction of mixed high-methoxyl pectin and kappa-carrageenan gels. *Food Hydrocolloids, 129*, Article 107647. https://doi.org/10.1016/j.foodhyd.2022.107647

Sow, L. C., Toh, N. Z. Y., Wong, C. W., & Yang, H. (2019). Combination of sodium alginate with tilapia fish gelatin for improved texture properties and nanostructure modification. *Food Hydrocolloids, 94*, 459–467. https://doi.org/10.1016/j.foodhyd.2019.03.041

Sun, J., Li, X., Xu, X., & Zhou, G. (2011). Influence of various levels of flaxseed gum addition on the water-holding capacities of heat-induced porcine myofibrillar protein. *Journal of Food Science, 76*(3), C472–C478. https://doi.org/10.1111/j.1750-3841.2011.02094.x

Tang, Q., Roos, Y. H., & Miao, S. (2024). Comparative studies of structural and thermal gelation behaviours of soy, lentil and whey protein: A pH-dependency evaluation. *Food Hydrocolloids, 146*, Article 109240. https://doi.org/10.1016/j.foodhyd.2023.109240

Tunick, M. H. (2011). Small-strain dynamic rheology of food protein networks. *Journal of Agricultural and Food Chemistry, 59*(5), 1481–1486. https://doi.org/10.1021/jf1016237

Vancauwenberghe, V., Verboven, P., Lammertyn, J., & Nicolaï, B. (2018). Development of a coaxial extrusion deposition for 3D printing of customizable pectin-based food simulant. *Journal of Food Engineering, 225*, 42–52. https://doi.org/10.1016/j.jfoodeng.2018.01.008

Wang, J., Jiang, Q., Huang, Z., Muhammad, A. H., Gharsallaoui, A., Cai, M., et al. (2024a). Rheological and mechanical behavior of soy protein-polysaccharide composite paste for extrusion-based 3D food printing: Effects of type and concentration of polysaccharides. *Food Hydrocolloids, 153*, Article 109942. https://doi.org/10.1016/j.foodhyd.2024.109942

Wang, W., Shen, M., Liu, S., Jiang, L., Song, Q., & Xie, J. (2018). Gel properties and interactions of Mesona blumes polysaccharide-soy protein isolates mixed gel: The effect of salt addition. *Carbohydrate Polymers, 192*, 193–201. https://doi.org/10.1016/j.carbpol.2018.03.064

Wang, K., Sun, H., Cui, Z., Wang, J., Hou, J., Lu, F., et al. (2024b). Synergistic effects of microbial transglutaminase and apple pectin on the gelation properties of pea protein isolate and its application to probiotic encapsulation. *Food Chemistry, 439*, Article 138232. https://doi.org/10.1016/j.foodchem.2023.138232

Wang, L., Zhang, M., Bhandari, B., & Gao, Z. (2016). Effects of malondialdehyde-induced protein modification on water functionality and physicochemical state of fish myofibrillar protein gel. *Food Research International, 86*, 131–139. https://doi.org/10.1016/j.foodres.2016.06.007

Xie, J., Bi, J., Nicolas, J., Christophe, B., Wang, F., & Lyu, J. (2024a). Dysphagia food: Impact of soy protein isolate (SPI) addition on textural, physicochemical and microstructural properties of peach complex gels. *Food Hydrocolloids, 154*, Article 110130. https://doi.org/10.1016/j.foodhyd.2024.110130

Xie, J., Lyu, J., Wang, F., Bai, L., & Bi, J. (2024b). Characterization of fruit pulp-soy protein isolate (SPI) complexes: Effect of superfine grinding. *Journal of Food Science, 89*(2), 1127–1142. https://doi.org/10.1111/1750-3841.16911

Xu, K., Wu, C., Fan, G., Kou, X., Li, X., Li, T., et al. (2023). Rheological properties, gel properties and 3D printing performance of soy protein isolate gel inks added with different types of apricot polysaccharides. *International Journal of Biological Macromolecules, 242*(Pt 1), Article 124624. https://doi.org/10.1016/j.ijbiomac.2023.124624

Zhang, D., Chen, D., & Campanella, O. H. (2024a). Effect of pH on the gelling properties of pea protein-pectin dispersions. *Food Hydrocolloids, 151*, Article 109731. https://doi.org/10.1016/j.foodhyd.2024.109731

Zhang, Q., Li, L., Lan, Q., Li, M., Wu, D., Chen, H., et al. (2019). Protein glycosylation: A promising way to modify the functional properties and extend the application in food system. *Critical Reviews in Food Science and Nutrition, 59*(15), 2506–2533. https://doi.org/10.1080/10408398.2018.1507995

Zhang, X., Wang, Y., Li, Z., Li, Y., & Qi, B. (2024b). Effects of polysaccharide type on the structure, interface behavior, and foam properties of soybean protein isolate hydrolysate-polysaccharide Maillard conjugates. *Food Hydrocolloids, 151*, Article 109801. https://doi.org/10.1016/j.foodhyd.2024.109801

Yi, J., Gan, C., Wen, Z., Fan, Y., & Wu, X. (2021). Development of pea protein and high methoxyl pectin colloidal particles stabilized high internal phase pickering emulsions for β-carotene protection and delivery. *Food Hydrocolloids, 113*, 106497. https://doi.org/10.1016/j.foodhyd.2020.106497.

Yu, Q., Li, X., Hu, J., Wang, W., & Bi, J. (2023). The effect of three pectin fractions variation on the browning of different dried apple products. *Food Hydrocolloids, 134*, 108052. https://doi.org/10.1016/j.foodhyd.2022.108052.

Zhang, B., Zhang, J., Yu, X., Peng, J., Pan, L., & Tu, K. (2022). Evaluation of the adsorption capacity and mechanism of soy protein isolate for volatile flavor compounds: Role of different oxygen-containing functional groups. *Food Chemistry, 386*, Article 132745. https://doi.org/10.1016/j.foodchem.2022.132745

Zhao, W., Xu, Y., Dorado, C., Bai, J., Chau, H. K., Hotchkiss, A. T., et al. (2024). Modification of pectin with high-pressure processing treatment of fresh orange peel before pectin extraction: Part II. The effects on gelling capacity and emulsifying properties of pectin. *Food Hydrocolloids, 149*, Article 109536. https://doi.org/10.1016/j.foodhyd.2023.109536

Zhou, M., Bi, J., Lyu, J., Chen, J., Wang, R., Liu, X., et al. (2021). Structural conversion of pectin fractions during heat processing in relation to the ability of inhibiting lipid digestion: A case study of hawthorn pectin. *Food Hydrocolloids, 117*, Article 1067721. https://doi.org/10.1016/j.foodhyd.2021.106721